RESEARCH ARTICLE

ADVANCED OPTICAL MATERIALS
www.advopticalmat.de

Reconfigurable Phase Profile Symmetry in Kirigami Metasurfaces

*Guobang Jiang, Ziyu Zhang, Yang Wang, Xing Li, Zhi Zheng, Yongfeng Mei, Lei Zhou, Shulin Sun, and Jizhai Cui**

The symmetry of the phase profile dictates how a metasurface manipulates electromagnetic waves. Altering that symmetry therefore directly enables wave control. Conventional mechanical methods such as elastic stretching and single-cell kirigami vary lattice spacings p_x, p_y and meta-atom orientation but leave the ordering unchanged, limiting the accessible symmetries. Here, supercell kirigami is introduced, where several phase-distinct meta-atoms are mounted on each rigid panel. During actuation, the panels stretch, rotate, and, crucially, reorder their meta-atom sequence. Guided by wallpaper group design principles, a variety of kirigami metasurfaces including rotating square and staggered rotating rectangle supercells, are fabricated, and experimentally realize five symmetry transitions, including the previously inaccessible *pmm* to *p4m* and *pmm* to *pmg* routes. Broadband measurements confirm wavefront conversions from dual to quad beams and redirection of reflected beams by 45°. Because the kirigami architecture is scale- and material-independent, the same strategy readily extends to higher frequency regimes. Operating at the phase map level rather than relying on resonator physics, this approach can also be applied to acoustic and thermal metasurfaces and even photonic crystals, opening broad prospects for reconfigurable wave devices.

1. Introduction

Metasurfaces consist of arrays of subwavelength meta-atoms arranged on a planar periodic lattice, have opened a versatile platform for electromagnetic (EM) wave manipulation, enabling beam steering,[1–5] holography,[6–8] imaging,[9–13] wireless communication,[14,15] and more. By prescribing each meta-atom a specific optical phase, through its geometry, material composition, or in-plane orientation, designers imprint a 2D phase profile that governs the outgoing wavefront.[16] This strategy has collapsed bulky optical elements into ultrathin layers capable of beam steering, focusing,[17,18] holography,[19–21] and polarization conversion,[22–25] promising compact, lightweight components across the radio-frequency,[26,27] terahertz,[28,29] infrared[30,31] and visible spectra.[32]

A metasurface's electromagnetic response is jointly governed by the intrinsic physical properties of its constituent resonant units and by the symmetry of its phase profile, while the former factor has been significantly explored.[33] Profiles that have high in-plane symmetry, such as the *pmm* pattern of a conventional grating or the *p4m* checkerboard used in beam splitters,[34] yield radiation patterns with correspondingly symmetric main lobes. Conversely, breaking reflection or rotation symmetries introduces phase profiles that drive asymmetric scattering or holographic images.[35] When the symmetry of the phase profile can be toggled on demand, the metasurface itself becomes

G. Jiang, Z. Zhang, Y. Wang, X. Li, Z. Zheng, Y. Mei, J. Cui
International Institute for Intelligent Nanorobots and Nanosystems & State Key Laboratory of Surface Physics
College of Intelligent Robotics and Advanced Manufacturing
Fudan University
Shanghai 200438, P. R. China
E-mail: jzcui@fudan.edu.cn

G. Jiang, Z. Zhang, Y. Wang, X. Li, Z. Zheng, Y. Mei, J. Cui
Zhejiang Key Laboratory of Extreme Environment Functional Materials
Yiwu Research Institute of Fudan University
Yiwu 322000, P. R. China

G. Jiang, Y. Mei, L. Zhou, S. Sun, J. Cui
Shanghai Key Laboratory of Metasurfaces for Light Manipulation
Fudan University
Shanghai 200433, P. R. China

Y. Mei
Shanghai Frontiers Science Research Base of Intelligent Optoelectronics and Perception
Institute of Optoelectronics
Fudan University
Shanghai 200438, P. R. China

L. Zhou
State Key Laboratory of Surface Physics and Key Laboratory of Micro and Nano Photonic Structures (Ministry of Education)
Fudan University
Shanghai 200433, P. R. China

S. Sun
Shanghai Engineering Research Centre of Ultra Precision Optical Manufacturing
Department of Optical Science and Engineering
College of Future Information Technology
Fudan University
Shanghai 200433, P. R. China

The ORCID identification number(s) for the author(s) of this article can be found under https://doi.org/10.1002/adom.202503586

DOI: 10.1002/adom.202503586

reconfigurable, allowing a single chip to switch between multiple beam manipulation function, effectively meeting the needs for practical applications.

Phase profile symmetry can be modulated by directly adjusting the phase imparted by each meta-atom. Electrical gating,[34] optical pumping,[36,37] thermo-optic tuning,[38] and magneto-optic control[39] exemplify this approach and offer high-speed operation, yet the underlying lattice remains fixed. These methods provide high tuning speed and rich multifunctionality. As an alternative approach, mechanical deformation reshapes the periodic lattice itself: stretching,[40,41] bending,[1] or twisting[42] redistributes meta-atoms in space while simultaneously altering their orientations. This circuit-free and inherently scale-independent route simplifies the entire system and lowers the component count, and may be particularly useful in low-speed, low-power applications such as deployable or space-based energy harvesting systems, where robustness and minimal wiring are more critical than fast response. In addition, mechanical strategies enable function switching through a single global actuation (for example, stretching or compressing the device), potentially reducing the number of independent control channels required. Typical mechanical tuning methods are based on substrate deformation, or origami and kirigami transformation,[43–46] realizing functionalities such as tunable beam bending or focusing,[47–50] frequency selection[51–53] and chirality switching.[54,55] For example, She et al. utilized elastic stretching methods to tune the lattice constant of the metalens, thereby changing the radial phase gradient.[40] Meanwhile, Wang et al. induced Miura-origami into mechanically reconfigurable metasurfaces, realizing tunable chirality.[56] Recent demonstrations using rotating square (RS) kirigami sheets showed that even a single mechanical degree of freedom can reverse the reflected beam direction via geometric phase modulation.[57–60] However, a comprehensive study of how diverse mechanical deformations govern phase profile symmetry is still missing, and the nearly infinite design space of kirigami patterns remain largely unexplored, leaving the full electromagnetic potential of mechanically reconfigurable metasurfaces largely unexplored.

Here we systematically map how mechanical deformation reshapes phase profile symmetry and, through carefully designed kirigami transformations, reveal a rich set of symmetry transition pathways that greatly extend the functionality of mechanically reconfigurable metasurfaces. Starting from a unit cell on a square lattice, we catalogue all 12 plane symmetry classes of the phase profile and the 78 mechanical transitions that connect them. By changing only the lattice constants p_x and p_y, pure substrate stretching reaches 21 of these routes; adding panel rotation, which simultaneously changes the meta-atom orientation, enables the classic single-cell RS kirigami to extend the count to 33. To reach the remaining pathways, we introduce supercell layouts combined with kirigami patterns in a variety of wallpaper groups (WG).[61] This design enables the reordering of the meta-atom sequence, providing a fourth mechanical degree of freedom that complements the tuning of p_x, p_y, and orientation. Using this strategy we demonstrate five representative transitions, including one unreachable previously. These devices convert wavefronts from a dual-beam to a beam pattern and redirect abnormal reflections from diagonal to parallel orientations, capabilities that existing mechanically reconfigurable metasurfaces have yet to achieve. Continued exploration of WG kirigami transformations promises access to all 78 symmetry transitions, establishing a foundation for symmetry-programmable, mechanically reconfigurable metasurfaces and further broadening the scope of mechanical wavefront control.

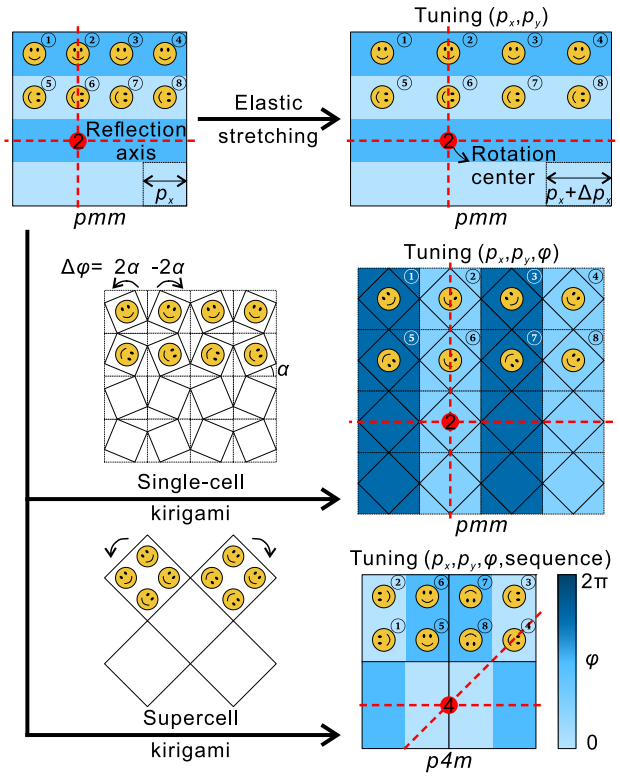

Figure 1. Modifying phase profile symmetry with three planar deformation schemes. Top panel, elastic stretching changes the lattice spacings p_x and p_y while meta-atom orientation and order remain fixed, so the phase profile keeps its *pmm* symmetry. Middle panel, single-cell rotating square kirigami varies p_x and p_y and the meta-atom orientation (geometric phase φ); the ordering is unchanged, and the symmetry stays *pmm*. Bottom panel, supercell kirigami adjusts p_x, p_y, φ, and also reorders the meta-atom sequence, converting the profile from *pmm* to *p4m*. Smiley icons represent meta-atoms whose orientation sets their geometric phase, visualized by the blue color scale. Numbers in circle ①-⑧ mark the sequence of meta-atoms. Red dashed lines and red dots denote reflection axes and rotation centers, respectively; the numbers 2 and 4 represent twofold and fourfold rotational symmetry, respectively.

2. Results

Mechanically reconfigurable metasurfaces can be actuated by elastic stretching, bending, or shape-morphing schemes such as origami and kirigami. Bending and most origami implementations tilt portions of the array out of the surface plane, increasing thickness and requiring additional optimization for the oblique incidence experienced by each meta-atom.[1,56] To avoid this complexity, we restrict our study to deformations that keep the array flat: axial stretching of the substrate and in-plane kirigami transformation, whose effects on the phase profile are summarized in **Figure 1**. The top panel of Figure 1 illustrates stretching. Each "smiley face" representing a meta-atom maintains its orientation,

so its geometric phase is fixed, while the spacing between adjacent units increases along the x-axis, tuning the lattice constants from (p_x, p_y) to ($p_x + \Delta p_x$, p_y). Here, the material's Poisson's ratio is neglected for simplicity. Because neither the phase imparted by individual meta-atoms nor their spatial sequence changes, the global phase profile retains its original *pmm* symmetry; only the grating periodicity is modified through the controllable adjustment of p_x (and, by symmetry, p_y when stretching is applied along y).

The middle panel of Figure 1 illustrates reconfiguration of a RS kirigami metasurface, a 2D tessellation of identical square panels separated by narrow cuts placed along their edges and hinged at the corners. In this kirigami design, each square can rotate relative to its neighbors. As neighboring panels turn in opposite directions (clockwise, CW, or counter-clockwise, CCW), the lattice deforms uniformly in both x and y axes, giving the pattern an auxetic, or negative-Poisson-ratio, response. Thus, a uniaxial stretch leads to synchronously elongation in the orthogonal direction, allowing simultaneous control of p_x and p_y. During the transformation each panel rotates through an angle α, and the geometric phase carried by its meta-atom changes by $\Delta\varphi = \pm 2\alpha$, with the sign set by the local sense of rotation (see detailed derivations in Note S1, Supporting Information). Although individual meta-atoms acquire different phase shifts and the lattice constants expand, the sequence of meta-atoms remains unchanged. Consequently, the reflection axes along x and y and the twofold rotation center at the square's midpoint are therefore preserved, so the global phase profile retains its *pmm* symmetry throughout the motion.

The bottom panel of Figure 1 illustrates that placing several meta-atoms with different initial phases on the same rotating square, thereby forming a supercell, fundamentally extends kirigami functionality. During the kirigami deformation, the lattice constants p_x and p_y and the meta-atom orientations all change, and, most importantly, the ordering of the meta-atoms is rearranged. This adjustment of four degrees rebuilds the phase profile: a metasurface that originally exhibited *pmm* symmetry with a single twofold rotation center is transformed into a *p4m* pattern possessing fourfold rotational symmetry and new reflection axes at 0° and 45°. Note that for various designs, the number of meta-atoms placed on one rotating square (or other kinds of kirigami units) would significantly influence the re-ordering procedure. Because the supercell RS design simultaneously controls p_x, p_y, orientation, and sequence, it potentially can access far more symmetry-switching pathways than conventional approaches and offers much richer dynamic modulation of the wavefront.

In the 2D plane there are seventeen wallpaper symmetry groups, each defined by a particular combination of the three fundamental symmetry operations: rotation, reflection, and glide reflection.[62] A phase profile built on a square lattice can realize twelve of these groups, which are discussed below; the remaining five (*p3*, *p3m1*, *p31m*, *p6*, and *p6m*) require a hexagonal lattice and are not considered here. Counting every possible conversion between two groups, and including the case in which the symmetry remains unchanged before and after deformation, there are ${}^{12}C_2+12 = 78$ distinct symmetry-transition pathways. **Figure 2** evaluates how far the two planar deformations, elastic stretching and single-cell RS kirigami, can navigate through this landscape. During elastic stretching, a uniaxial strain deforms the lattice uniformly, tuning the lattice constant along the stretch direction while leaving each meta-atom's orientation and ordering intact. Figure 2a shows that reflections perpendicular to the stretch axis (0° and 90°) together with the associated twofold rotation centers survive, whereas reflections at 45° and 135° and the fourfold rotation center are lost. Glide reflections follow the same preservation or loss pattern as their corresponding reflection axes. Applying these rules yields 21 symmetry group transition routes, as plotted in Figure 2b (Figure S1, Supporting Information for full analysis). Although stretching is the simplest actuation mode, it accesses only a small fraction of the full transition set.

In the RS kirigami, each lattice cells are cut into a rotating square, allowing neighboring panels to rotate in opposite directions during transformation, which produces local phase shifts of $\pm 2\alpha$ and enlarges both lattice constants. In the single-cell configuration, each rotating square panel carries either one meta-atom or a set of meta-atoms that all share the same initial phase, so the panel functions as a single electromagnetic cell. To trace how the kirigami transformation edits symmetry, we mark three high-symmetry points of the square lattice: Γ at the center of a cell, M at the vertex where four cells meet, and X and Y at the midpoints of a horizontal or vertical cell edge. Figure 2c shows that every reflection or rotation element passing through Γ is preserved, those at M lose the fourfold rotation and the reflections along 0° and 90° but keep the twofold rotation, and all rotational symmetry at X or Y disappears. Glide reflections display a position-dependent response that is detailed in Figure S2 (Supporting Information). We also note, as discussed in Figure S3 (Supporting Information), that a rare combination of phase periodicity and rotation angle can introduce unexpected symmetry elements in special conditions. Enumerating all possibilities gives 33 symmetry-transition routes as shown in Figure 2d (Figure S4, Supporting Information for full analysis). We note that the 21 routes produced by elastic stretching are entirely contained within these 33 transitions, confirming that single-cell RS kirigami enlarges the transition space achievable by pure stretching. In the general case, every arrow in Figure 2b,d points from the upper-left toward the lower-right of the diagram, indicating a change from higher to lower symmetry or, at best, the maintenance of the original symmetry. This overall downward trend reflects the fact that both stretching and single-cell RS deformation typically break reflection or rotational elements without creating new ones. Only in special situations can the reverse of a listed path produce a symmetry gain. For example, stretching a rectangle along its short side until it becomes a square reinstates fourfold rotational symmetry and moves the system upward in the diagram. Such symmetry-enhancing inverses are therefore possible but require finely tuned geometry and are not representative of the general behavior captured by the forward arrows.

Existing elastic stretching and single-cell RS kirigami adjust at most the lattice spacings p_x, p_y, and the orientation α of the meta-atoms, and neither approach can access the full set of 78 symmetry-transition pathways, highlighting the need for additional mechanical degrees of freedom to achieve full symmetry programmability. If several meta-atoms with different initial phases are integrated on the same rotating panel, the kirigami motion also reorders their spatial sequence. Sequence permutation becomes an additional mechanical degree of freedom,

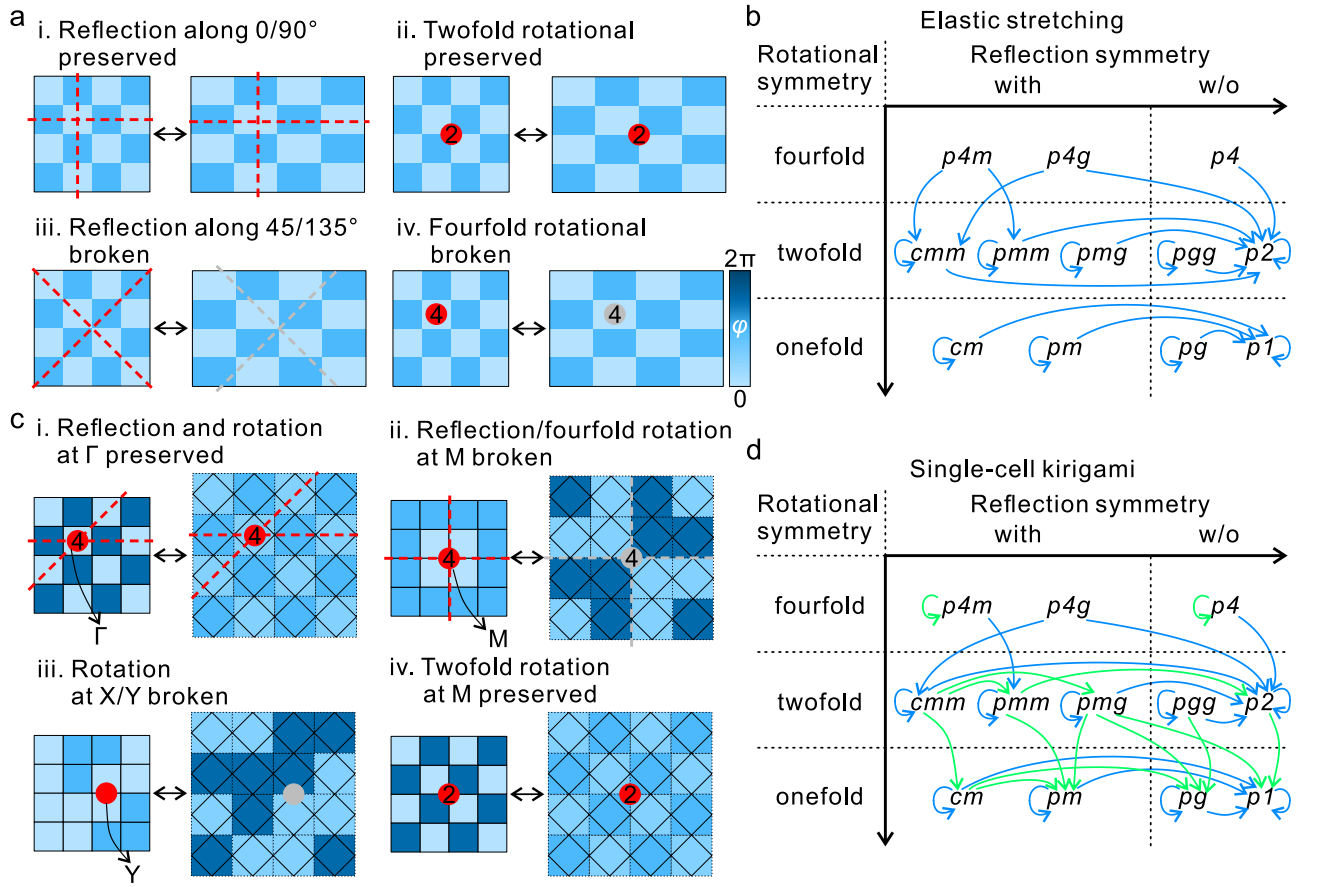

Figure 2. Symmetry evolution under elastic stretching and single-cell kirigami deformation schemes. a) Effect of uniaxial stretching on reflection and rotation symmetries. Blue tiles represent the phase profile; broken elements are marked by gray dashed lines or dots. b) 21 symmetry-transition pathways accessible with stretching, grouped by rotational order (fourfold, twofold, onefold) and by the presence or absence of reflection symmetry. c) Effect of single-cell kirigami on reflection and rotation symmetries. High-symmetry points are labelled Γ (cell center), X and Y (edge centers), and M (lattice corners). d) 33 symmetry-transition pathways produced by single-cell kirigami. Blue arrows correspond to the stretching routes in (b), while green arrows denote additional paths unlocked by rotation-induced phase shifts.

promising far broader control over the phase profile than is possible with spacing and orientation alone.

To demonstrate sequence-guided symmetry control, we first designed locally responding meta-atoms with a radius of 2.1 mm that maintain relatively high (>0.8) polarization conversion rate from 12.5 to 16 GHz, allowing for kirigami-based control of geometric phase (see detailed information in Figure S5, Supporting Information). We then 3D-printed kirigami panels and connected them with rotational hinges (Figures S6–S8, Supporting Information). As **Figure 3a** illustrates, each rotating panel contains four groups of meta-atoms, with every group consisting of four identical elements; the phase of each group can be set independently, allowing four distinct phase values on a single panel. In the undeformed state, the array presents a grating-like phase profile with *pmm* symmetry, which produces clear scattering signatures and allows both symmetry reduction and symmetry elevation to be tracked during deformation.

We mapped this grating profile onto a supercell RS sheet in which the two upper groups of meta-atoms on each panel share one phase while the two lower groups differ by π. Figure 3a demonstrates the three stages of kirigami transformation: the initial state ($\alpha = 0°$), an intermediate state ($\alpha = 45°$), and the terminal state ($\alpha = 90°$). The whole transformation process is shown in Video S1 (Supporting Information). Serial numbers indicated on the 8 meta-atom groups trace the change of their relative positions during the kirigami transformation. The accompanying phase maps in Figure 3b depict the phase profiles and their symmetry evolution: the initial profile contains two orthogonal reflection axes and a twofold rotation cent (i.e., *pmm* symmetry); after kirigami transformation ($\alpha = 90°$) the reordered sequence yields a checkerboard pattern with four reflection axes and a fourfold rotation center (reflection axes at 0°, 45°, 90°, and 135°), that is, *p4m* symmetry. The supercell implementation therefore achieves a symmetry-increasing transition from *pmm* to *p4m*. In the elastic-stretching and single-cell RS schemes, this conversion appears only when an arrow in Figure 2 is traced in the reverse direction (from its lower-symmetry endpoint back to its higher-symmetry origin), so it is practically challenging to access in conventional mechanically reconfigurable metasurfaces. By providing direct access to this upward symmetry pathway, our approach greatly enlarges the design space for dynamic wavefront engineering and paves the way for devices that can toggle between

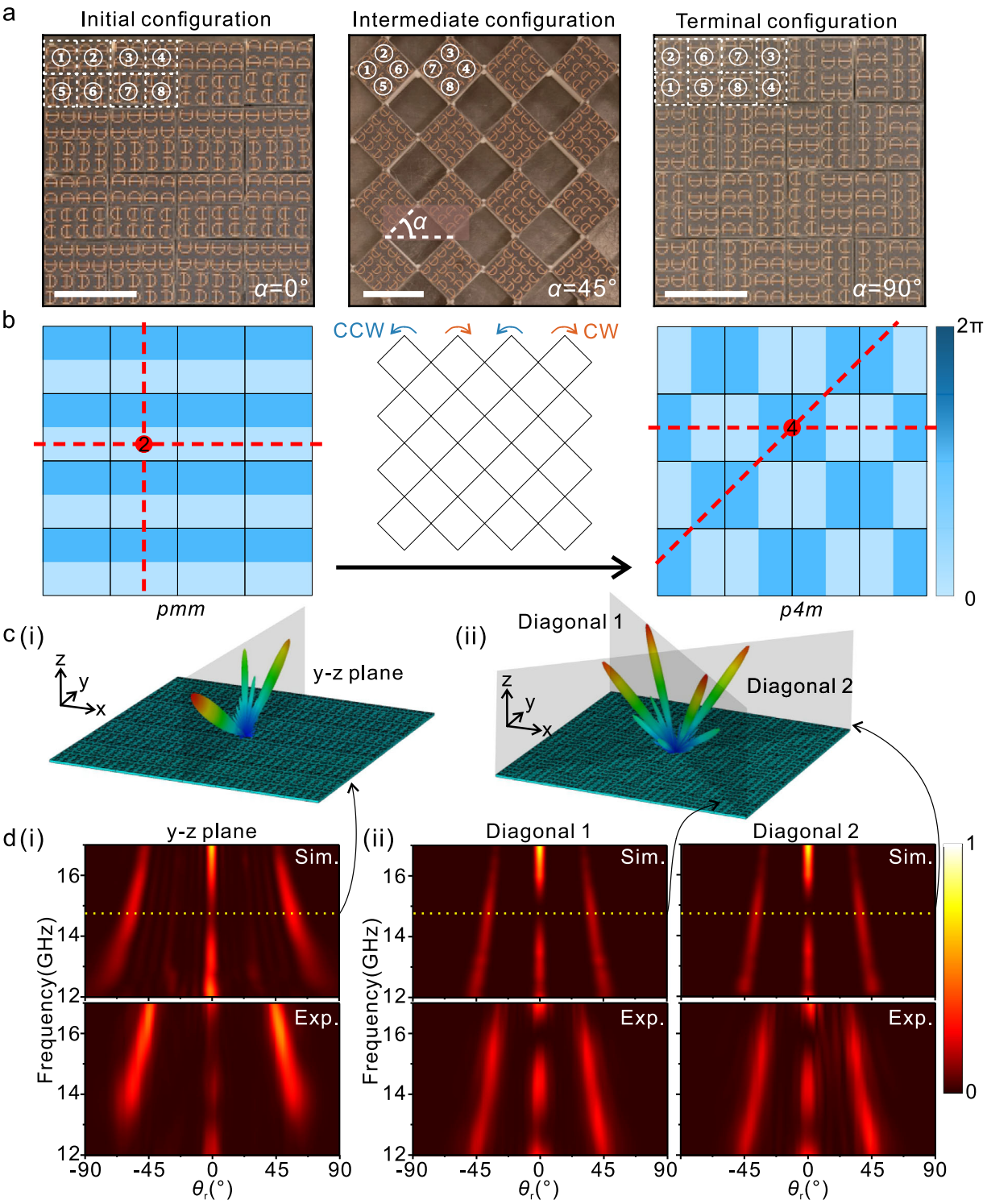

Figure 3. Experimental demonstration of a *pmm*-to-*p4m* symmetry transition using a supercell rotating square kirigami metasurface. a) From left to right, photographs of the fabricated kirigami metasurface in the initial ($\alpha = 0°$), intermediate ($\alpha = 45°$) and terminal ($\alpha = 90°$) configurations. Numbers label the four meta-atom groups on two neighboring panels, showing how their order changes during actuation. Scale bars, 30 mm. b) Phase profiles corresponding to the three configurations in (a). The initial grating has *pmm* symmetry. CW and CCW panel rotations reposition the reflection axes and rotation center and raise the symmetry to *p4m*, producing a checkerboard phase map in the terminal state. c) Simulated far-field scattering patterns at 14.75 GHz. In the initial undeformed state i), the metasurface reflects two beams within the y-z plane under normal incidence, whereas in the terminal state ii) it redirects four beams into two diagonal planes (highlighted in grey). d) Frequency-angle intensity maps for the planes indicated in (c). Simulation (upper panels) and measurement (lower panels) agree well for both the y-z plane in the initial configuration i) and the two diagonal planes in the terminal configuration ii), confirming the dual-beam to quad-beam conversion.

fundamentally different operating regimes on a single, integrated platform.

Beam-steering measurements confirm the functional impact of the new symmetry. Figure 3ci and ii show simulated far-field patterns for the initial and terminal states. The *pmm* grating launches two equal beams on the y-z plane, whereas the *p4m* checkerboard generates four balanced beams along two diagonal planes. In order to obtain a comprehensive understanding of the deformation process, the simulated far-field scattering patterns throughout the whole transformation route of the metasurface are shown in Figure S9 (Supporting Information). The gradual evolution of the reflected main lobes reveals a competition between different diffraction modes induced by the changing phase symmetry and air-gap geometry. Additionally, we provide the reflection efficiency as a function of deformation angle in Figure S10 (Supporting Information) to directly show the influence of the air gaps that appear during stretching. The result proves that the influence of the discretized phase profile on the efficiency is slight and could be ignored. Figure 3d compares simulations with experiments: panel 3d(i) plots EM responses at y-z plane for the kirigami at the initial state, panel 3d(ii) shows the responses at two diagonal planes 1 and 2 at the terminal state. In each case the measured lobes match the simulations well, and the discrepancies are probably due to fabrication tolerances and measurement conditions (see Methods). The reflection angles could also be predicted by generalized Snell's Law (see details in Note S2, Supporting Information), in good agreement with both simulations and experiments. The supercell RS metasurface therefore shifts from two-beam to four-beam operation, a transformation beyond the reach of conventional mechanically reconfigurable metasurfaces.

To probe symmetry pathways that remain inaccessible, we combine the supercell concept with WG kirigami—an approach that begins by selecting one of the 17 planar wallpaper symmetries and then positioning the cuts so that both the compact and the deployed sheet strictly follow that symmetry.[61] Because every wallpaper group can be realized in this manner, the method provides a systematic way to embed or remove any combination of rotational centers, reflection axes, and glide-reflection axes that are permitted in 2D space, and to switch among them during the kirigami transformation (examples shown in Figure S11, Supporting Information).[61] This added capability for tailoring lattice symmetry complements the supercell approach and is expected to unlock phase profile transitions that stretching or single-cell RS designs cannot reach. Building on this idea, we adopt a staggered rotating rectangle (SRR) pattern, a tessellation of rectangles whose long axes alternate by 90° in each column (Figure S11, Supporting Information). In the SRR kirigami pattern, all panels in one row rotate CW while the panels in the next row rotate CCW. This architecture preserves the mechanical advantages of the RS design, acting as a new form of meta-atom sequence permutation.

Figure 4a shows the fabricated SRR supercell at three deformation states α = (0°, 45°, and 90°). The whole transformation process is shown in Video 2. Each SRR panel carries two groups of meta-atoms. The two groups can be assigned independent geometric phases, while each group contains four identical meta-atoms. Eight numbered meta-atoms trace the opposite rotating directions of successive rows: elements 1–4 roll CW, whereas 5–8 roll CCW. The initial phase map (Figure 4b, left) is a grating tilted 45°, giving *pmm* symmetry with reflection axes along 45°/135° and a twofold rotation center at their crossing. After kirigami transformation the combined changes in orientation and ordering rebuild the map into a nearly horizontal dual-phase profile with one reflection axis and an off-axis twofold rotation center, producing overall *pmg* symmetry (Figure 4b, right). Such *pmm*-to-*pmg* transition lies entirely outside the catalogue of routes shown in Figure 2b,d, neither among the 21 paths attainable by elastic stretching nor within the 33 reachable through single-cell RS kirigami (even when those paths are traced in reverse). The SRR supercell therefore introduces a genuinely new symmetry-switching pathway that conventional planar reconfiguration schemes cannot provide, further expanding the accessible portion of the full 78-path landscape.

The electromagnetic consequences follow the symmetry change. Simulated far-field patterns in Figure 4c(i) show that the undeformed grating launches two equal beams in the diagonal plane that is 45° relative to the x-z plane. After deformation the *pmg* profile redirects the beams into the x-z plane, as shown in Figure 4c(ii). Figure S12 (Supporting Information) illustrates the simulated far-field scattering modes of the metasurface throughout the whole deformation route for a better understanding of the transformation process. The deformation-dependent reflection efficiency, shown in Figure S13 (Supporting Information), is used to quantify the effect of air gaps introduced during stretching of the SRR metasurface. The result shows that the discretized phase profile does not significantly affect the efficiency. Figure 4d compares simulations with measurements: panel 4d(i) plots the angular spectrum of the EM responses in the diagonal plane at the initial configuration (0°), whereas panel 4d(ii) shows that the x-z plane at the terminal configuration (90°). In both cases the measured lobes reproduce the predicted envelopes, confirming accurate phase delivery throughout the motion. Thus, the SRR supercell functions as a steerable grating whose main beams direct from the diagonal to the parallel plane, a response that remains unattainable in previously reported mechanically reconfigurable metasurfaces.

Beyond the RS and SRR demonstrations, three additional prototypes are designed and fabricated based on this concept. The first is a gradient phase profile mapped on a supercell RS (full deformation process in Video S3, Supporting Information), realizing a symmetry transition pathway of *pm*-to-*cm*. The anomalous reflected single beam is tuned to a dual-beam pattern in this case, where details can be found in Figures S14 and S15 (Supporting Information). The second design is a grating along the horizontal direction patterned on a rotating rectangle (RR) kirigami (full deformation process in Figure S11 and Video S4, Supporting Information), enabling a symmetry transition pathway of *pmm*-to-*cmm*. Here, the reflected dual-beam is changed to quad-beam, as demonstrated in Figures S16 and S17 (Supporting Information). The last one is a grating along the vertical direction, also on a RR kirigami (full deformation process in Video S5, Supporting Information). This design enables a symmetry transition pathway of *pmm*-to-*pmm*, which only alters the reflection angle of the reflected dual-beam (Figures S18 and S19, Supporting Information). Of the five symmetry pathways (summarized in Figure S20, Supporting Information) we have experimentally realized, three (*pmm*-to-*p4m*, *pmm*-to-*cmm*, and *pm* to *cm*) correspond to moving opposite to the arrows plotted in Figure 2b,d; in other

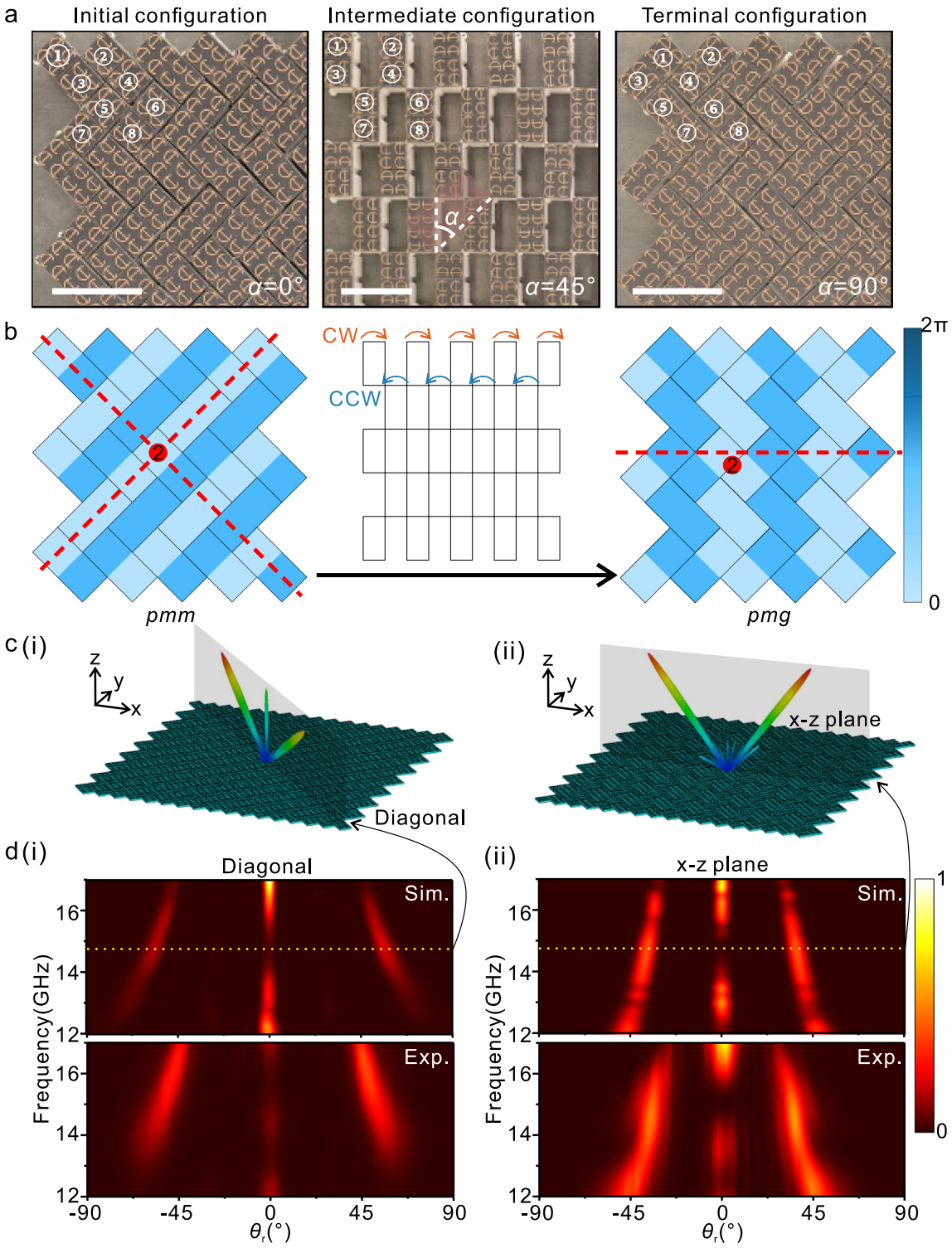

Figure 4. Experimental demonstration of the *pmm*-to-*pmg* transition in a supercell staggered rotating rectangle kirigami metasurface. a) From left to right, photographs of the metasurface in the initial ($\alpha = 0°$), intermediate ($\alpha = 45°$), and terminal ($\alpha = 90°$) configurations. Numbers label eight meta-atom groups on four adjacent panels, illustrating their reordered positions during actuation. Scale bars, 30 mm. b) Calculated phase profiles for the three states in (a). The undeformed sheet in the initial configuration shows *pmm* symmetry with reflection axes along 45° and 135°. CW and CCW panel rotations shift the symmetry elements, producing a grating-like phase map with *pmg* symmetry in the terminal configuration. c) Simulated far-field patterns at 14.75 GHz. The initial profile i) reflects two beams into a single diagonal plane, whereas the terminal profile ii) redirects the beams into the x-z plane, highlighted in grey. d) Frequency-angle intensity maps for the planes indicated in (c). Simulation (upper) and experiment (lower) agree for both the diagonal plane in the initial state i) and the x-z plane in the terminal state ii), confirming the grating's steerable dual-beam response.

words, they start from a lower-symmetry group and climb back to a higher one that ordinary stretching or single-cell RS deformation can reach only when the process is run in reverse. One of the remaining routes, *pmm*-to-*pmg*, is completely absent from those charts and thus cannot be produced at all with the conventional schemes. Demonstrating both upward and previously unreachable moves on the symmetry map confirms that supercell layouts combined with WG-guided kirigami eliminate longstanding limits in mechanical metasurface tuning. This broadened control palette allows a single device to toggle among multiple, functionally distinct phase architectures on demand and provides a systematic path toward exploiting the full set of 78 theoretical transitions for next-generation adaptive wavefront engineering.

3. Conclusion

In summary, we have presented a mechanically reconfigurable metasurface architecture that unites supercell layouts with WG kirigami designs to unlock symmetry-transition pathways that lie beyond the reach of conventional stretching or single-cell designs. Starting from a full enumeration of the twelve planar symmetry classes available to unit cells in a square lattice, we analyzed how uniaxial stretching and single-cell RS kirigami affect the phase profile, though constrained by a fixed meta-atom sequence. Introducing supercells lifts this constraint by adding sequence permutation as a fourth mechanical degree of freedom alongside the tuning of p_x, p_y and orientation. Guided by WG theory, we then selected three kirigami patterns and fabricated metasurfaces that realize five distinct symmetry transitions, including the $pmm \rightarrow p4m$ and $pmm \rightarrow pmg$ routes demonstrated with the RS and SRR supercells. Numerical simulations together with broadband microwave measurements confirm that these transitions translate into wavefront transformations such as dual-beam to four-beam splitting or a change of reflection direction of grating lobes from the diagonal to the parallel plane, performances unattainable in previously reported mechanically reconfigurable metasurfaces.

The framework is intrinsically scalable and versatile. Functionalities other than beam steering can also be realized with the proposed strategy, for example, a switchable lens and a switchable vortex-beam generator (Figures S21 and S22, Supporting Information). WG kirigami catalogues cover all seventeen wallpaper groups, making the approach compatible with square, hexagonal, and oblique lattices;[61] moving from microwaves to terahertz or even visible frequencies, therefore requires only a change in meta-atom dimensions and material choice. Future work can couple the mechanical cuts with micro-actuators[47] to achieve millisecond-level switching, integrate electronic biasing to combine mechanical and electrical tuning, and employ inverse-design algorithms[45] to select optimal supercell-kirigami pairings for a target electromagnetic function. Because the method manipulates symmetry at the level of the phase map, without changing the local resonator physics, the same design logic can, in principle, be transferred to acoustic or thermal metasurfaces, and even to photonic-crystal slabs, enabling adaptive beam steering, dynamic holography, and reconfigurable topological transport across a broad spectrum of wave-based technologies.

4. Experimental Section

Fabrication of Metasurfaces: The kirigami reconfigurable metasurface consists of deformable substrate units and resonant meta-atoms adhered to their upper surfaces. Each meta-atom is affixed to the deformable unit at a specific position and orientation, and the substrate units are assembled in a manner that allows the metasurface to deform along a predetermined kirigami pathway. The deformable substrate units are fabricated with resin using 3D printing, with a refractive index of ≈1.25. Each meta-atom comprises a three-layer structure: the top layer is a patterned copper resonator with a specific geometry, the middle layer is a 1.5 mm-thick FR4 dielectric ($\epsilon_n = 2.6$), and the bottom layer is a continuous copper film that acts as a ground plane reflector. Due to the presence of this copper backing, incident EM waves from above cannot penetrate through to the resin deformable substrate, effectively isolating the resin layer from contributing to the EM responses. Therefore, the influence of the resin on the wave propagation can be considered negligible.

Numerical Simulations: In all numerical simulations, the metasurfaces are vertically illuminated by linearly polarized (LP) EM waves. The resulting far-field scattering patterns and in-plane intensity distributions correspond to the electric field intensity $|E|^2$ of the reflected left-handed circularly polarized (LHCP) component. All data were normalized with respect to the total incident energy.

Experimental Measurements: All experimental measurements are conducted using LP incident waves, with the reflected LHCP signals being detected. A reference measurement is performed by replacing the metasurface sample with a flat metallic plate of identical size and shape to the sample. The mirror-reflected signal from this metallic plate is used to normalize the experimental data. The assembled metasurface is vertically mounted on a PMMA board, which is nearly transparent to EM waves within the measured frequency band. An LP horn antenna connected to port 1 of a vector network analyzer (VNA) is used as the transmitter, while an LHCP horn antenna connected to port 2 of the VNA served as the receiver. The transmitting horn is fixed at a distance of 1.8 m from the metasurface, positioned at the same height as the metasurface center, and aligned such that the line connecting the horn antenna and metasurface center is normal to the metasurface plane. The receiving horn is mounted on a movable arm at the same height and distance (1.8 m) as the transmitting horn, and could rotate in an arc around the center of the metasurface. By recording the S21 parameter at various angular positions of the receiving horn, the reflected EM field intensity distribution is obtained.

Error Analysis: Several factors contribute to the discrepancies between the experimental results and the simulations. i) Material parameters: In the simulations, the permittivity of the dielectric substrate was set to 3, and the metallic layer was modeled as a perfect electric conductor (PEC). In the experiments, the actual permittivity of the dielectric slightly deviates from 3, and the metal is copper with finite conductivity. These differences can lead to blue- or red-shifts in the reflection spectra. ii) Antenna gain profile: The horn the gain spectrum of the horn antennas used in the experiments is not perfectly flat but follows a smooth curve over 8–18 GHz range used in the experiment. which may cause the relative reflection intensity received at different wavelengths deviating from the simulated results. iii) Measurement configuration: To suppress unwanted scattering, microwave-absorbing foam was placed on both sides of the metallic frame holding the metasurface. While this configuration significantly reduces spurious peaks in the reflection spectra, it also makes it almost impossible to reliably detect signals corresponding to large reflection angles (near ±90°), which affects the measured side lobes iv) Fabrication tolerances: The kirigami metasurface was assembled using 3D-printed components. Small variations in the height and dimensions of the meta-atoms inevitably arise from the printing and assembly processes and introduce an additional propagation phase in reflection, which is not captured in the idealized simulations.

Supporting Information

Supporting Information is available from the Wiley Online Library or from the author.

Acknowledgements

This work is supported by the National Key Technologies R&D Program of China (2022YFA1404700, 2022YFA1207000, and 2020YFA0710100), the National Natural Science Foundation of China (52101214, 12374344, 12221004, and 62192771), and Science and Technology Commission of Shanghai Municipality (21YF1401600, 21ZR1403500, 24520750200, 24CL2900200), Shanghai Rising-Star Program (24QA2700700), and Shanghai Talent Programs.

Conflict of Interest

The authors declare no conflict of interest.

Data Availability Statement

The data that support the findings of this study are available in the supplementary material of this article.

Keywords

kirigami, microwave, plane symmetry, reconfigurable metasurfaces, wavefront shaping

Received: December 4, 2025
Revised: December 18, 2025
Published online: January 5, 2026

[1] X. Zhuang, W. Zhang, K. Wang, Y. Gu, Y. An, X. Zhang, J. Gu, D. Luo, J. Han, W. Zhang, *Light Sci Appl* **2023**, *12*, 14, https://doi.org/10.1038/s41377-022-01046-6.
[2] A. M. H. Wong, G. V. Eleftheriades, *Metasurface, Physical Review X* **2018**, *8*, 011036.
[3] S. Sun, Q. He, S. Xiao, Q. Xu, X. Li, L. Zhou, *Nat. Mater.* **2012**, *11*, 426, https://doi.org/10.1038/nmat3292.
[4] S. Sun, K.-Y. Yang, C.-M. Wang, T.-K. Juan, W. T. Chen, C. Y. Liao, Q. He, S. Xiao, W.-T. Kung, G.-Y. Guo, L. Zhou, D. P. Tsai, *Nano Lett.* **2012**, *12*, 6223, https://doi.org/10.1021/nl3032668.
[5] N. Yu, P. Genevet, M. A. Kats, F. Aieta, J.-P. Tetienne, F. Capasso, Z. Gaburro, *Science* **2011**, *334*, 333, https://doi.org/10.1126/science.1210713.
[6] C. Liu, H. Wang, R. Zhao, Y. Lei, S. Dong, Y. Cai, W. Zhou, Y. Wang, L. Huang, K.-M. Xu, *Photonics Res.* **2024**, *12*, 2158, https://doi.org/10.1364/PRJ.523778.
[7] Q. Cao, N. Zhang, A. Chong, Q. Zhan, *Nat. Commun.* **2024**, *15*, 7821.
[8] N. A. Rubin, A. Zaidi, A. H. Dorrah, Z. Shi, F. Capasso, J. metasurfaces, *Sci. Adv.* **2021**, *7*, abg7488.
[9] E. Choi, G. Kim, J. Yun, Y. Jeon, J. Rho, S.-H. Baek, *Nat. Photonics* **2024**, *18*, 848, https://doi.org/10.1038/s41566-024-01450-x.
[10] J. Zhou, F. Tian, J. Hu, Z. L. Shi, V. G. Godinez, D. P. Tsai, Z. Liu, *Adv. Mater.* **2024**, *36*, 2402751, https://doi.org/10.1002/adma.202402751.
[11] C. Chen, W. Song, J.-W. Chen, J.-H. Wang, Y. H. Chen, B. Xu, M.-K. Chen, H. Li, B. Fang, J. Chen, H. Y. Kuo, S. Wang, D. P. Tsai, S. Zhu, T. Li, *Light Sci Appl* **2019**, *8*, 99, https://doi.org/10.1038/s41377-019-0208-0.
[12] M. Pan, Y. Fu, M. Zheng, H. Chen, Y. Zang, H. Duan, Q. Li, M. Qiu, Y. Hu, *Light Sci Appl* **2022**, *11*, 195, https://doi.org/10.1038/s41377-022-00885-7.
[13] A. Zaidi, N. A. Rubin, M. L. Meretska, L. W. Li, A. H. Dorrah, J.-S. Park, F. Capasso, *Nat. Photonics* **2024**, *18*, 704, https://doi.org/10.1038/s41566-024-01426-x.
[14] Z. X. Wang, J. W. Wu, H. Xu, J. Y. Dai, S. Liu, Q. Cheng, T. J. Cui, *Adv. Sci. (Weinh)* **2024**, *11*, 2403624, https://doi.org/10.1002/advs.202403624.
[15] X. G. Zhang, Y. L. Sun, B. Zhu, W. X. Jiang, Q. Yu, H. W. Tian, C.-W. Qiu, Z. Zhang, T. J. Cui, *Light Sci Appl* **2022**, *11*, 126, https://doi.org/10.1038/s41377-022-00817-5.
[16] A. I. Kuznetsov, M. L. Brongersma, J. Yao, M. K. Chen, U. Levy, D. P. Tsai, N. I. Zheludev, A. Faraon, A. Arbabi, N. Yu, D. Chanda, K. B. Crozier, A. V. Kildishev, H. Wang, J. K. W. Yang, J. G. Valentine, P. Genevet, J. A. Fan, O. D. Miller, A. Majumdar, J. E. Fröch, D. Brady, F. Heide, A. Veeraraghavan, N. Engheta, A. Alù, A. Polman, H. A. Atwater, P. Thureja, R. Paniagua-Dominguez, et al., *ACS Photonics* **2024**, *11*, 816, https://doi.org/10.1021/acsphotonics.3c00457.
[17] R. Zhang, Y. Guo, X. Li, Q. He, Q. Zhang, F. Zhang, M. Xu, M. Wang, M. Pu, X. Luo, *Adv. Opt. Mater.* **2023**, *12*, 2300009, https://doi.org/10.1002/adom.202300009.
[18] C. Zhang, L. Chen, Z. Lin, J. Song, D. Wang, M. Li, O. Koksal, Z. Wang, G. Spektor, D. Carlson, H. J. Lezec, W. Zhu, S. Papp, A. Agrawal, *Light Sci Appl* **2024**, *13*, 23, https://doi.org/10.1038/s41377-023-01330-z.
[19] H. Yang, P. He, K. Ou, Y. Hu, Y. Jiang, X. Ou, H. Jia, Z. Xie, X. Yuan, H. Duan, *Light Sci Appl* **2023**, *12*, 79, https://doi.org/10.1038/s41377-023-01125-2.
[20] B. Chen, S. Yang, J. Chen, J. Wu, K. Chen, W. Li, Y. Tan, Z. Wang, H. Qiu, K. Fan, C. Zhang, H. Wang, Y. Feng, Y. He, B. Jin, X. Wu, J. Chen, P. Wu, *Light Sci Appl* **2023**, *12*, 136, https://doi.org/10.1038/s41377-023-01177-4.
[21] G. Zheng, H. Muhlenbernd, M. Kenney, G. Li, T. Zentgraf, S. Zhang, *Nat. Nanotechnol.* **2015**, *10*, 308.
[22] J. R. Nolen, A. C. Overvig, M. Cotrufo, A. Alù, *Nat. Nanotechnol.* **2024**, *19*, 1627, https://doi.org/10.1038/s41565-024-01763-6.
[23] H. Luo, J. Luo, Z. Zhang, C. Wu, Q. Li, W. Liu, R. Peng, M. Wang, H. Li, Y. Lai, *Light Sci Appl* **2024**, *13*, 262, https://doi.org/10.1038/s41377-024-01605-z.
[24] S. Hu, L. Wei, Y. Long, S. Huang, B. Dai, L. Qiu, S. Zhuang, D. Zhang, *Opt. Express* **2024**, *32*, 6963, https://doi.org/10.1364/OE.514410.
[25] J. P. Balthasar Mueller, N. A. Rubin, R. C. Devlin, B. Groever, F. Capasso, *Phys. Rev. Lett.* **2017**, *118*, 113901, https://doi.org/10.1103/PhysRevLett.118.113901.
[26] S. Qu, Y. Hou, P. Sheng, *Proc Natl Acad Sci* **2021**, *118*, 2110490118, https://doi.org/10.1073/pnas.2110490118.
[27] C. Qian, B. Zheng, Y. Shen, L. Jing, E. Li, L. Shen, H. Chen, *Nat. Photonics* **2020**, *14*, 383, https://doi.org/10.1038/s41566-020-0604-2.
[28] C. Wang, Y. Tan, Y. Wen, S. Zhao, K. Yu, J. Sun, J. Zhou, *ACS Photonics* **2024**, *11*, 1236, https://doi.org/10.1021/acsphotonics.3c01762.
[29] Z. Zhang, Z. Wang, C. Zhang, Z. Yao, S. Zhang, R. Wang, Z. Tian, J. Han, C. Chang, J. Lou, X. Yan, C. Qiu, *Adv. Mater.* **2024**, *36*, 2308453, https://doi.org/10.1002/adma.202308453.
[30] J. King, C. Wan, T. J. Park, S. Deshpande, Z. Zhang, S. Ramanathan, M. A. Kats, *Nat Photon* **2023**, *18*, 74, https://doi.org/10.1038/s41566-023-01324-8.
[31] Y. Chen, X. Zheng, F. Liu, W. Pan, Z. Wang, M. Liu, Z. Zhu, Y. Wang, L. Li, Q. He, S. Sun, L. Zhou, *Opt. Express* **2023**, *31*, 34112, https://doi.org/10.1364/OE.502028.
[32] A. H. Dorrah, N. A. Rubin, A. Zaidi, M. Tamagnone, F. Capasso, *Nat. Photonics* **2021**, *15*, 287, https://doi.org/10.1038/s41566-020-00750-2.
[33] Q. Chen, G. Qu, J. Yin, Y. Wang, Z. Ji, W. Yang, Y. Wang, Z. Yin, Q. Song, Y. Kivshar, S. Xiao, *Nat. Nanotechnol.* **2024**, *19*, 1000, https://doi.org/10.1038/s41565-024-01636-y.
[34] T. J. Cui, M. Q. Qi, X. Wan, J. Zhao, Q. Cheng, *Light Sci Appl* **2014**, *3*, 218, https://doi.org/10.1038/lsa.2014.99.
[35] H. Chu, X. Xiong, Y.-J. Gao, J. Luo, H. Jing, C.-Y. Li, R. Peng, M. Wang, Y. Lai, *Sci. Adv.* **2021**, *7*, abj0935, https://doi.org/10.1126/sciadv.abj0935.

[36] J. Hu, Z. Liang, P. Zhou, L. Liu, G. Hu, M. Ye, *Adv. Opt. Mater.* **2024**, *12*, 2400594, https://doi.org/10.1002/adom.202400594.
[37] H. Wang, Z. Hu, J. Deng, X. Zhang, J. Chen, K. Li, G. Li, *Sci. Adv.* **2024**, *30*, adk3882, https://doi.org/10.1126/sciadv.adk3882.
[38] T. Guo, Z. Zhang, Z. Lin, J. Tian, Y. Jin, J. Evans, Y. Xu, S. He, *Nat. Nanotechnol.* **2024**, *19*, 1635, https://doi.org/10.1038/s41565-024-01756-5.
[39] W. Yang, J. Qin, J. Long, W. Yan, Y. Yang, C. Li, E. Li, J. Hu, L. Deng, Q. Du, L. Bi, *Nat. Electron.* **2023**, *6*, 225, https://doi.org/10.1038/s41928-023-00936-w.
[40] A. She, S. Zhang, S. Shian, D. R. Clarke, F. Capasso, *Sci. Adv.* **2018**, *4*, aap9957, https://doi.org/10.1126/sciadv.aap9957.
[41] I. M. Pryce, K. Aydin, Y. A. Kelaita, R. M. Briggs, H. A. Atwater, *Nano Lett.* **2010**, *10*, 4222, https://doi.org/10.1021/nl102684x.
[42] S. Liu, S. Ma, R. Shao, L. Zhang, T. Yan, Q. Ma, S. Zhang, T. J. Cui, *Sci. Adv.* **2022**, *8*, abo1511, https://doi.org/10.1126/sciadv.abo1511.
[43] C. Coulais, A. Sabbadini, F. Vink, M. van Hecke, *Nature* **2018**, *561*, 512, https://doi.org/10.1038/s41586-018-0541-0.
[44] B. Liu, J. L. Silverberg, A. A. Evans, C. D. Santangelo, R. J. Lang, T. C. Hull, I. Cohen, *Nat. Phys.* **2018**, *14*, 811, https://doi.org/10.1038/s41567-018-0150-8.
[45] G. P. T. Choi, L. H. Dudte, L. Mahadevan, *Nat. Mater.* **2019**, *18*, 999, https://doi.org/10.1038/s41563-019-0452-y.
[46] Y. Zheng, K. Chen, Y. Feng, *Ann. Phys.* **2024**, *536*, 2400213, https://doi.org/10.1002/andp.202400213.
[47] C. L. Smart, T. G. Pearson, Z. Liang, M. X. Lim, M. I. Abdelrahman, F. Monticone, I. Cohen, P. L. McEuen, *Science* **2025**, *386*, 1031, https://doi.org/10.1126/science.adr2177.
[48] L. Xu, X. Wang, Y. Kim, T. C. Shyu, J. Lyu, N. A. Kotov, *ACS Nano* **2016**, *10*, 6156;
[49] Y. Zheng, K. Chen, W. Yang, L. Wu, K. Qu, J. Zhao, T. Jiang, Y. Feng, *Adv. Funct. Mater.* **2021**, *32*, 2107699, https://doi.org/10.1002/adfm.202107699.
[50] C. Qi, A. M. H. Wong, *IEEE Transactions on Antennas and Propagation* **2022**, *70*, 7300, https://doi.org/10.1109/TAP.2022.3164931.
[51] K. Fuchi, A. R. Diaz, E. J. Rothwell, R. O. Ouedraogo, J. Tang, *J. Appl. Phys.* **2012**, *111*, 084905, https://doi.org/10.1063/1.4704375.
[52] X. Yao, M. Li, S. He, L. Jing, C. Li, J. Tao, X. Hui, F. Gao, J. Song, H. Chen, Z. Wang, *Research* **2024**, *7*, 0367, https://doi.org/10.34133/research.0367.
[53] G. Wang, D. Li, W. Liao, T. Liu, X. Li, Q. An, Z. Qu, *Adv. Mater.* **2024**, *36*, 2408216, https://doi.org/10.1002/adma.202408216.
[54] R. Phon, H. Jeong, S. Lim, *Adv. Mater. Technol.* **2022**, *7*, 2101706, https://doi.org/10.1002/admt.202101706.
[55] Z. Liu, Y. Xu, C.-Y. Ji, S. Chen, X. Li, X. Zhang, Y. Yao, J. Li, *Adv. Mater.* **2020**, *32*, 1907077, https://doi.org/10.1002/adma.201907077.
[56] Z. Wang, L. Jing, K. Yao, Y. Yang, B. Zheng, C. M. Soukoulis, H. Chen, Y. Liu, *Adv. Mater.* **2017**, *29*, 1700412, https://doi.org/10.1002/adma.201700412.
[57] G. Jiang, Y. Wang, Z. Zhang, W. Pan, Y. Chen, Y. Wang, X. Chen, E. Song, G. Huang, Q. He, S. Sun, J. Cui, L. Zhou, Y. Mei, *Nat. Commun.* **2025**, *16*, 1660, https://doi.org/10.1038/s41467-025-56211-3.
[58] Y. Wang, Y. Shi, L. Li, Z. Zhu, M. Liu, X. Jin, H. Li, G. Jiang, J. Cui, S. Ma, Q. He, L. Zhou, S. Sun, *Nanomaterials* **2025**, *15*, 61, https://doi.org/10.3390/nano15010061.
[59] W. Luo, S. Xiao, Q. He, S. Sun, L. Zhou, *Adv. Opt. Mater.* **2015**, *3*, 1102, https://doi.org/10.1002/adom.201500068.
[60] L. Huang, X. Chen, H. Mühlenbernd, G. Li, B. Bai, Q. Tan, G. Jin, T. Zentgraf, S. Zhang, *Nano Lett.* **2012**, *12*, 5750, https://doi.org/10.1021/nl303031j.
[61] L. Liu, G. P. T. Choi, L. Mahadevan, *Proc R Soc A* **2021**, *477*, 20210161, https://doi.org/10.1098/rspa.2021.0161.
[62] D. Schattschneider, *The American Mathematical Monthly* **2018**, *85*, 439, https://doi.org/10.1080/00029890.1978.11994612.